



Modelling of air entrainment during pouring of metal castings

Seyyed Hojjat Majidi & Christoph Beckermann

To cite this article: Seyyed Hojjat Majidi & Christoph Beckermann (2017) Modelling of air entrainment during pouring of metal castings, International Journal of Cast Metals Research, 30:5, 301-315, DOI: [10.1080/13640461.2017.1307624](https://doi.org/10.1080/13640461.2017.1307624)

To link to this article: <http://dx.doi.org/10.1080/13640461.2017.1307624>



Published online: 29 Mar 2017.



Submit your article to this journal [↗](#)



Article views: 158




View related articles [↗](#)



View Crossmark data [↗](#)



Modelling of air entrainment during pouring of metal castings

Seyyed Hojjat Majidi  and Christoph Beckermann

Department of Mechanical and Industrial Engineering, The University of Iowa, Iowa City, IA, USA

ABSTRACT

Air entrainment during mould filling is major source of oxide inclusions in metal castings. A model is developed to predict the location and rate of air entrainment as part of a standard mould filling simulation. The local air entrainment rate is calculated as a function of the turbulent kinetic energy and the magnitude of the normal velocity gradient of the liquid metal at the liquid–air interface. The model is validated through comparisons with experimental air entrainment measurements for a plunging water jet. It is then applied to study the effect of gating system design and pouring parameters on air entrainment in steel casting. Air entrainment is found to be reduced for a metal stream from the ladle that is centred above the pouring cup or the use of an offset step pouring basin, low head heights, high flow rates, a pressurised gating system and bottom ingates.

ARTICLE HISTORY

Received 16 December 2016
Accepted 10 March 2017

KEYWORDS

Air entrainment; inclusions; mould filling; turbulent kinetic energy; casting simulation

Introduction

Oxide inclusions are among the most commonly reported defects in ferrous and non-ferrous castings. They affect the surface quality, machinability and mechanical performance of a cast part. Inclusions form when the liquid metal comes into contact with oxygen during mould filling. In low-alloy steel castings, the reaction between the deoxidised steel and oxygen is responsible for the formation of round reoxidation inclusion, while in light metals, including aluminium alloy castings, solid oxide films are generated. In ductile iron castings, dross inclusions (magnesium silicates) form when the magnesium and silicon in the melt react with oxygen. The removal of inclusions from castings, if possible, can be very costly. Numerous efforts have been made to minimise inclusions in castings, but methods to predict inclusion formation and generally valid gating design guidelines are currently not available.

Air entrainment during mould filling is the main source of the oxygen that is consumed in inclusion formation. In free surface flows, air is entrained at surface discontinuities. Such surface discontinuities are created, for example, by a liquid jet plunging into a pool (Figure 1), breaking waves, or a hydraulic jump, in which a fast moving liquid discharges into a low velocity atmosphere. In the plunging jet case, the air is entrained in a thin layer around the perimeter of the jet where it enters the pool. The air entrainment rate depends primarily on the jet velocity, diameter and turbulence level. Air entrainment commences only above a certain critical jet velocity

(approximately 1 m s^{-1} for water). For jet velocities at the point of impact of the order of 5 m s^{-1} , relative air entrainment rates of one cubic metre of air per cubic metre of liquid are easily reached.

During mould filling, several types of free surface flows can occur that entrain air. Liquid metal plunging into the sprue, jets emanating from ingates or falling over edges inside of the casting cavity and returning waves in runners are some of the most important examples of such flows. The oxygen in that entrained air will almost immediately react with elements in the liquid metal to form solid, liquid and/or gaseous oxides. While the gaseous oxides can often escape from the casting cavity, liquid and solid oxides are transported with the liquid metal and ultimately end up as inclusions in the solidified casting.

Simulation software is now routinely used in the foundry industry to model not only solidification, but also the filling of the mould with the liquid metal. Such filling simulations are usually one-sided, meaning that they only calculate the flow of the metal but not of the air. Hence, air entrainment is not predicted. Even if the air were included in the calculations, air entrainment and the movement of air bubbles would be difficult to simulate directly because these phenomena occur on such a small scale that they cannot be resolved by a typical computational mesh used in a casting simulation (of the order of millimetres). Therefore, approximate or sub-grid models have been developed, as reviewed next, that attempt to calculate air entrainment as part of a one- or



Figure 1. Air bubbles near a plunging liquid water jet by 'Jesse Belden (NUWC) and Tadd T. Truscott (BYU)' [1].

two-sided computational fluid dynamics simulation on a relatively coarse mesh, i.e. one that does not resolve the turbulent eddies and air bubbles directly.

The model developed by Moraga et al. [2] assumes that bubbles are entrained beneath the free surface once the downward liquid velocity perpendicular to the interface exceeds the bubble rise velocity. The model is combined with an expression, derived from experimental measurements, to predict the bubbly flow below the impact location of a plunging jet [3]. This model is only capable of predicting the location of air entrainment. Studies have pointed out that air entrainment at surface discontinuities is associated with large values of the turbulent kinetic energy [4,5]. Xiang et al. [5] developed a model to calculate the air entrainment rate as a function of the local turbulent kinetic energy and the jet velocity at the location of the surface discontinuity. A critical velocity criterion is used to detect the onset of air entrainment. Ma et al. [6] predict the rate of air entrainment as a function of the turbulent kinetic energy and the normal velocity gradient of the liquid at the liquid–air interface. Air is entrained only when the normal velocity at the interface increases in the direction normal to the interface. The model is used together with a turbulent two-phase computational fluid dynamics code to predict bubble void fractions in the bulk liquid. Good agreement is achieved between predicted void fraction profiles and experimental measurements for hydraulic jumps [7] and plunging jets [8]. Souder and Hirt [9,10] determine the air entrainment rate from the difference between the turbulent kinetic energy and the energy of surface stabilising forces, i.e. surface tension and gravity. As in the study by Ma et al. [6], a separate turbulence model is

solved to predict the mean flow characteristics, including the local turbulent kinetic energy. Comparisons between predicted air entrainment rates and experimental data collected for plunging jets, drop shafts, hydraulic jumps and spillways show good overall agreement.

While the above studies are aimed at predicting air entrainment in any kind of free surface flow, some models have been developed specifically for application in mould filling simulations for metal casting. In aluminium casting, the liquid metal is covered with a thin solid oxide film, and surface turbulence has been found to be the main cause of the entrainment of oxide films into the bulk liquid [11]. Lai et al. [12,13] compare the modelled instantaneous free surface area of the melt to the instantaneous free surface area assuming the liquid metal fills the mould quiescently. The difference between these two free surface areas is used to determine the oxide entrainment magnitude. Although this model appears to work for simple geometries, it is difficult to apply to complex filling systems. Furthermore, the model does not provide insight into the location of air entrainment. Several studies have pointed out the importance of non-dimensional numbers for predicting the free surface breakup in filling of aluminium castings [13,14]. While the Weber number is found to be a proper criterion for vertical running systems, the Froude number has been suggested to be more appropriate for horizontal running systems. Such distinctions are difficult to apply to complex mould geometries. Determining the magnitude of air entrainment solely based on non-dimensional numbers also fails to account for the local turbulence intensity of the flow and the physical scale of the entraining phenomena [13]. Several criteria have been suggested for predicting entraining events in aluminium casting based on velocity vectors, free surface normals and liquid volume fractions in free surface cells [13,15,16]. The entraining events are classified into three categories: flows with colliding fronts, shear flows and impinging flows [16,17]. While these models provide insight into the location of entrainment, they fail to quantify the amount of entrained air or inclusions/oxide films.

In the present study, the sub-grid model of Ma et al. [6–8] is implemented into a standard (one-sided) casting filling simulation code to calculate local air entrainment rates. An approximate method is proposed to estimate the turbulent kinetic energy without solving a separate turbulence model. The model is validated and calibrated by comparing predicted air entrainment rates for a plunging water jet with previously obtained experimental data. The model capabilities are then demonstrated by simulating the flow in typical casting filling systems and calculating the air entrainment rates. It is shown how different pouring conditions and gating designs affect the rate of entrained air and, hence, the formation of inclusions.

Model description

The air entrainment calculations described here are performed as part of a standard casting filling simulation [18]. The filling simulation calculates the melt velocity by solving the Navier–Stokes equations at each time step, while the geometry of the free surface at each time step is determined using a volume tracking method (VOF method). This section describes the model for predicting the air entrainment rate at free surfaces.

The present model is based on the recent work of Ma et al. [6–8], in which the local air entrainment rate is calculated as a function of the turbulent kinetic energy and the magnitude of the normal velocity gradient at the liquid–air interface. Turbulence inside the liquid results in disturbances on the free surface. As shown in Figure 2, for a turbulent eddy of size l_e and velocity u_e the disturbance size δ is of the order of

$$\delta \sim \frac{u_e^2}{2g} \rightarrow \delta \sim \frac{k}{g} \quad (1)$$

where k ($\text{m}^2 \text{s}^{-2}$) is the turbulent kinetic energy and g (m s^{-2}) is the gravitational acceleration [19]. Assuming that all of the air entrainment occurs in a layer close to the interface where the disturbances exist, the volumetric rate of entrained air per unit interfacial area, q (m s^{-1}), can be estimated by the air quantity passing the inward surface Γ_e in Figure 2 as [6]

$$q(\mathbf{x}) \propto u_n(\mathbf{x} + \mathbf{n}C_1\delta) - u_n(\mathbf{x}) \quad (2)$$

where u_n is the liquid velocity normal to the liquid–air interface, \mathbf{n} is the unit normal vector towards the liquid, C_1 is a non-dimensional constant of $O(1)$, and \mathbf{x} is an arbitrary point on the interface.

Using the definition of a derivative

$$\frac{\partial u_n}{\partial n} = \lim_{\delta \rightarrow 0} \frac{u_n(\mathbf{x} + \mathbf{n}C_1\delta) - u_n(\mathbf{x})}{C_1\delta} \quad (3)$$

and combining Equations (1)–(3), the rate of air entrainment per unit interfacial area can be estimated as

$$q(\mathbf{x}) = \frac{C_{ent}}{g} k(\mathbf{x}) \frac{\partial u_n}{\partial n}(\mathbf{x}) \quad (4)$$

where C_{ent} is a dimensionless entrainment coefficient that is still to be determined and $(\partial u_n / \partial n)$ is the normal derivative of the normal component of the liquid velocity at the interface (s^{-1}). The sign of $(\partial u_n / \partial n)$ determines whether air is entrained or not:

- $(\partial u_n / \partial n) < 0$: normal velocity decreases in the direction normal to the interface; the interface is moving with a higher velocity than the inward surface; therefore, air will be detrained rather than entrained.
- $(\partial u_n / \partial n) = 0$: normal velocity remains constant in the direction normal to the interface; the interface is moving with the same velocity as the inward surface; air will not be entrained or detrained.
- $(\partial u_n / \partial n) > 0$: normal velocity increases in the direction normal to the interface; the inward surface is moving with a higher velocity than the interface; the disturbances are drawn into the liquid and then break up into bubbles.

Hence, only positive values of $(\partial u_n / \partial n)$ will lead to air entrainment. Equation (4) indicates that the rate of air entrainment per unit interfacial area is a function of the disturbance size and the normal derivative of the normal velocity at the interface. Earlier studies have pointed out the importance of turbulent kinetic energy and differential velocity in determining the rate of air entrainment [21].

The volumetric air entrainment rate, Q_a ($\text{m}^3 \text{s}^{-1}$), can be calculated by integrating the rate of air entrainment per unit interfacial area over the interfacial area

$$Q_a = \iint_{A_i} q dA \quad (5)$$

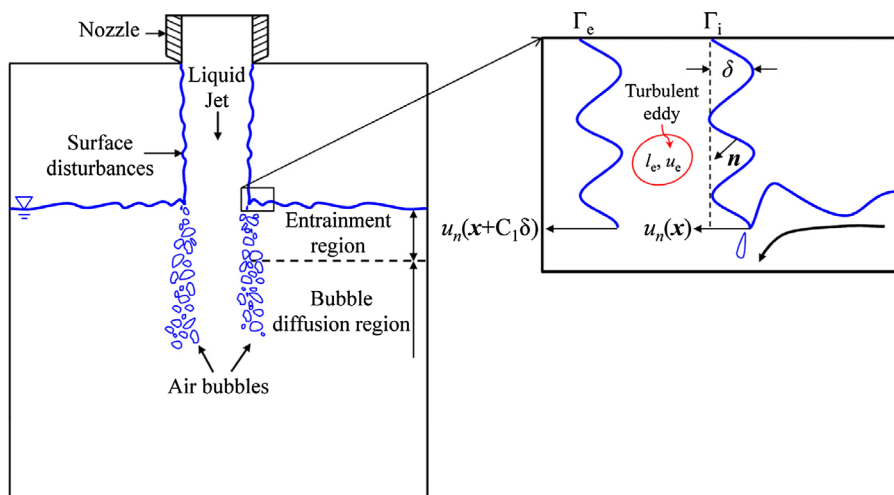


Figure 2. Air entrainment along the periphery of a liquid jet plunging into a quiescent pool. Adapted from Refs. [6] and [20].

where A_s is the interfacial area.

Turbulent kinetic energy

The local turbulent kinetic energy, k ($\text{m}^2 \text{s}^{-2}$), is the kinetic energy per unit mass associated with all eddies within the turbulent flow and is defined as

$$k = \frac{1}{2}(\overline{u_x'^2} + \overline{u_y'^2} + \overline{u_z'^2}) \quad (6)$$

where u_x' , u_y' and u_z' are the fluctuating components of the velocity. They are defined as

$$u_x' = u_x - \overline{u_x} \quad (7a)$$

$$u_y' = u_y - \overline{u_y} \quad (7b)$$

$$u_z' = u_z - \overline{u_z} \quad (7c)$$

where the overbar indicates an average. In fluid mechanics, turbulence models are used for estimating the mean flow characteristics of turbulent flows. These turbulence models calculate the local turbulent kinetic energy of the flow field by solving additional equations. When using turbulence models, temporal average values are used. The method suggested here does not require any turbulence model, and for averaging purposes, it uses spatial averaging instead of temporal averaging. The spatial average is calculated as the mean value of a variable over a 27 point computational stencil in 3 dimensions. For the velocity components, this can be expressed as

$$\overline{u_x} = \frac{\sum_{p=1}^{27} u_{x,p}}{27} \quad (8a)$$

$$\overline{u_y} = \frac{\sum_{p=1}^{27} u_{y,p}}{27} \quad (8b)$$

$$\overline{u_z} = \frac{\sum_{p=1}^{27} u_{z,p}}{27} \quad (8c)$$

Normal derivative of the normal component of velocity at the interface

In the casting filling simulation, the free surface is tracked using the VOF method. In this method, the computational cells in which the liquid–air interface resides have a certain liquid volume fraction, α_f which varies from zero to unity across the interface. Using the liquid volume fraction, the normal vector at the interface and the normal velocity can be calculated, respectively, as

$$\mathbf{n} = \frac{\nabla \alpha_f}{|\nabla \alpha_f|} \quad (9)$$

$$u_n = \mathbf{u} \cdot \mathbf{n} \quad (10)$$

Then, the normal derivative of the normal velocity at the interface can be calculated from

$$\frac{\partial u_n}{\partial n} = \mathbf{n} \cdot \nabla u_n \quad (11)$$

with the turbulent kinetic energy (k) and normal derivative of the normal velocity ($\partial u_n / \partial n$) being calculated as described above, the entrainment coefficient (C_{ent}) is the only unknown in Equation (4). It is determined in the next section by comparing predictions of the air entrainment model with experimental measurements for water.

Model calibration and validation for a plunging water jet

Air entrainment associated with a circular water jet plunging into a quiescent pool has been studied experimentally by numerous researchers [20,22]. Their experimental data are used here to validate the present air entrainment model and to determine the entrainment coefficient, C_{ent} . The plunging water jet simulations were performed for a tank with length and width of 203.2 mm (8"). The quiescent pool has a height of 203.2 mm. The jet enters the computational domain at the top through an inlet that represents a nozzle. The falling height h_j is the distance between the nozzle exit and the impact location (Figure 3(a)). An overflow is designed to keep the falling height constant during a simulation. A base case result for a plunging water jet is shown in Figure 3, with the velocity distribution in the jet and the pool plotted in Figure 3(a). The computed local air entrainment rate per unit of entrainment coefficient contours plotted in Figure 3(b) indicate that, as expected, air entrainment is predicted to take place at the periphery of the jet where it impacts the pool. The calculated variation of the total air entrainment rate (per unit of entrainment coefficient) in the entire computational domain is shown in Figure 3(c). It can be seen that after the initial impact of the jet, the total air entrainment rate reaches a steady state, although some fluctuations persist. For the comparison with experimental measurements shown below, the total air entrainment rate per unit of entrainment coefficient Q_a / C_{ent} of the plunging jet is taken as the average value during the steady-state period, as illustrated in Figure 3(c). This average value is divided by the volumetric flow rate of the water Q_w to obtain the relative air entrainment rate per unit of entrainment coefficient for a plunging jet.

Before determining the entrainment coefficient and comparing the present model to experiments, a computational mesh dependency study was performed. In all cases, a uniform mesh was utilised that consists of cubes of a certain side length. Figure 4 shows that for the plunging water jet base case just discussed, the calculated Q_a / C_{ent} values experience a slight decrease as the mesh is refined from a 3.6 to a 1.6 mm grid spacing. This relatively minor mesh dependency was deemed acceptable. At least four grid points are required to numerically

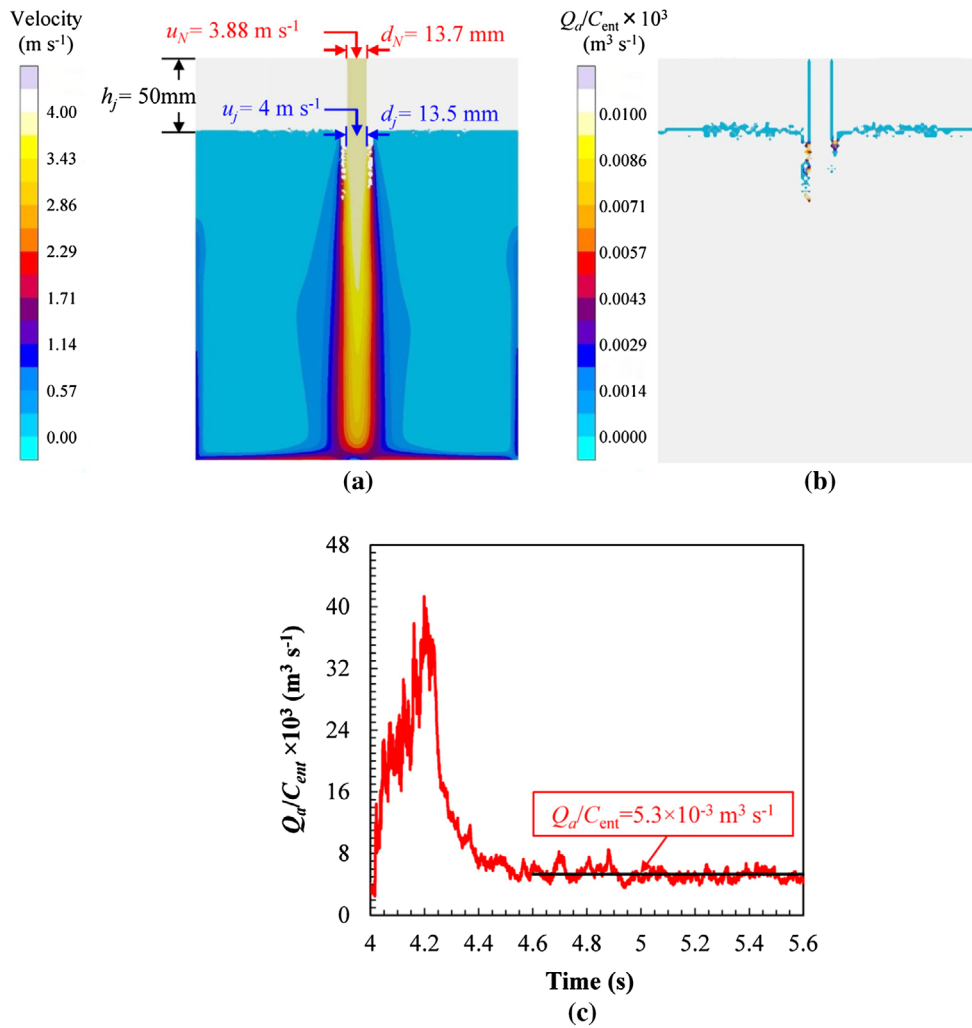


Figure 3. Base case plunging water jet simulation with $u_j = 4 \text{ m s}^{-1}$, $d_j = 13.5 \text{ mm}$, and $h_j = 50 \text{ mm}$: (a) velocity contours at $t = 5 \text{ s}$ at the mid plane, (b) local air entrainment rate per unit of entrainment coefficient contours at $t = 5 \text{ s}$ at the mid plane and (c) total air entrainment rate per unit of entrainment coefficient as a function of time.

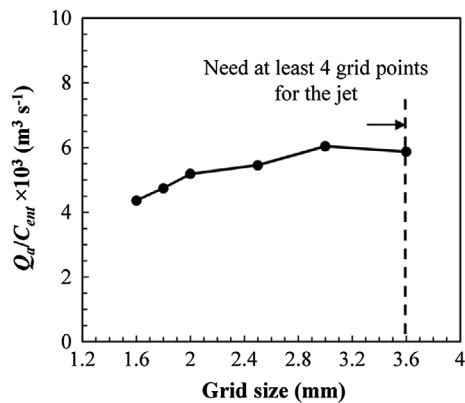


Figure 4. Calculated air entrainment rate per unit of entrainment coefficient as a function of grid spacing for the plunging water jet base case.

resolve the jet itself. A uniform grid spacing of 2 mm is used for all of the following plunging water jet cases.

Studies have shown that, in addition to the turbulence level, the rate of air entrainment in plunging jets is primarily a function of the jet velocity u_j and diameter d_j at

the location of the impact with the pool [3,20,22]. In the simulations, they are controlled by the jet velocity and diameter at the nozzle (inlet) u_N and d_N , respectively, as well as by the falling height between the nozzle and the pool h_j . All of these variables are indicated in Figure 3(a). They are related by

$$u_N = \sqrt{u_j^2 - 2gh_j} \quad (12)$$

$$d_N = d_j \sqrt{\frac{u_j}{u_N}} \quad (13)$$

Simulations were conducted for jet velocities in the range $1 \leq u_j (\text{m s}^{-1}) \leq 6$ and jet diameters in the range $10 \leq d_j (\text{mm}) \leq 25$. The lower limit of the jet velocity range corresponds approximately to the onset of air entrainment, while the upper limit is a transition point above which air entrainment is no longer controlled by interface disturbances [3].

The air entrainment coefficient, C_{ent} was determined by comparing the predicted steady-state relative air

entrainment rates to experimental measurements. In this study, the following experimental correlation for a low turbulence plunging jet proposed by Ervine and Ahmed (1982), as reported in Ref. [20], is used in the calibration

$$\frac{Q_a}{Q_w} = 0.003 Fr_j^2 \quad (14)$$

where the jet Froude number at impact, Fr_j , is defined as

$$Fr_j^2 = \frac{u_j^2}{gd_j} \quad (15)$$

By minimising the root mean square error between the predicted relative air entrainment rate values and the above experimental correlation, the entrainment coefficient was determined to be equal to $C_{ent} = 0.039$. As shown in Figure 5(a), the resulting agreement between measured and predicted relative air entrainment rates is excellent over the entire Froude number range investigated in the present study.

The experimental correlation indicates that the relative air entrainment rate varies with the square of the plunging jet velocity at impact. Figure 5(b) shows that this trend is correctly predicted by the present model. For a jet velocity of $u_j = 1 \text{ m s}^{-1}$, the air entrainment rate is measured and predicted to become negligibly small. For a jet velocity of $u_j = 6 \text{ m s}^{-1}$ (and $d_j = 13.5 \text{ mm}$), the relative air entrainment rate approaches unity. The experimental correlation specifies that the relative air entrainment rate is inversely proportional to the jet diameter. Figure 5(c) shows that the present computations predict this trend as well. Overall, the good agreement between measurements and predictions, for a single value of the air entrainment coefficient, lends considerable confidence to the present model and computations.

Next the effect of the turbulence level of the plunging jet on the relative air entrainment rate is studied using the experimental data of Ervine et al. [22]. The turbulence intensity is defined as

$$I = \frac{\sqrt{u_N'^2}}{u_N} \quad (16)$$

As mentioned earlier, u_N is the velocity of the jet at the nozzle, and the prime and the overbar indicate the fluctuating and mean components of the velocity, respectively. In the present simulations, turbulence was induced by applying the following time-dependent sinusoidal velocity profile at the nozzle (inlet)

$$u_N = \bar{u}_N + u_N' = \bar{u}_N [1 + I \times \sin(\omega t)] \quad (17)$$

where ω and t are frequency and time, respectively. In accordance with the experimental study of Ervine et al. [22], the frequency was set to $\omega = 65\pi$ and the turbulence intensity to $I = 0.05 = 5\%$. Simulations were

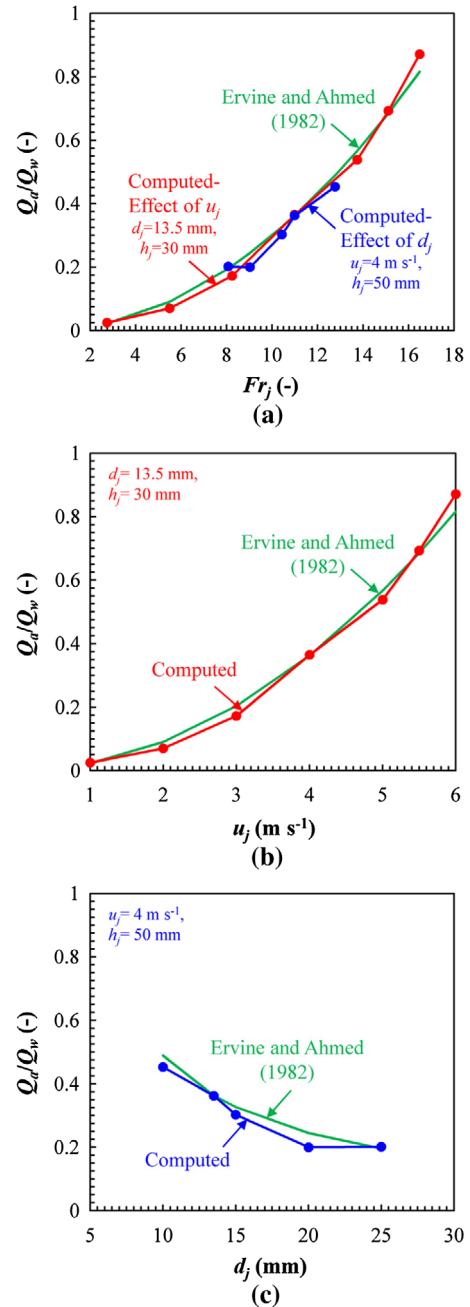


Figure 5. Relative air entrainment rate for a low turbulence plunging jet as a function of (a) Froude number, (b) jet velocity at impact and (c) jet diameter at impact.

conducted for four different mean jet velocities. Figure 6 shows that good agreement is obtained between the measured and predicted relative air entrainment rates for a turbulent plunging jet. For a turbulence intensity of 5%, the relative air entrainment rate increases by a factor of approximately three relative to the low turbulence data of Ervine and Ahmed (1982). Clearly, turbulence is a major factor in air entrainment.

Air entrainment during mould filling

The present model is now applied to investigate the effect of various gating system designs and pouring parameters on air entrainment during mould filling. In

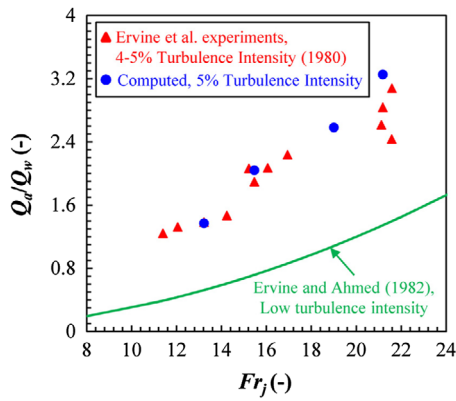


Figure 6. Comparison between measured and predicted relative air entrainment rates for a turbulent plunging jet.

all cases, the cast part is represented by a rectangular block with a length and width of 304.8 mm (12") and a height of 177.8 mm (7"). The filling simulations were conducted using a commonly available casting simulation code [18] in which the present air entrainment model was implemented. The material properties were taken from the standard database of the software and correspond to a low alloy steel in a furan sand mould. Though the simulations are performed for steel casting, the final comparison between different gating systems and pouring parameters should not be affected by the metal type. The pouring temperature was set to 1600 °C (2912 °F). A uniform mesh consisting of cubes with a side length of 3 mm was used in all simulations.

Table 1 lists all of the cases studied. First, a cone-shaped pouring cup on top of a vertical down sprue with a cylindrical well and a bottom ingate is investigated. The effects of the gating system pressurisation state, fill time (flow rate), location of the impact of the stream from the ladle and the head height above the cup are studied. Second, air entrainment for an offset step pouring basin is examined. Third, the effect of the location of the ingate is studied.

Cone pouring cup with bottom ingate

The geometry for the gating system with a cone-shaped pouring cup and a bottom ingate is provided in Figure 7. The casting has a pour weight of 156 kg (344 lb). First, a non-pressurised and pressurised gating system are compared. As shown in Figure 8, the non-pressurised gating system features an ingate that has twice the cross-sectional area of the sprue (1:2 sprue to ingate area ratio). For the pressurised gating system, the ingate is made smaller in an attempt to keep the upstream part of the gating system filled with liquid metal during the majority of the filling process; here the area ratio is 1:0.6 (sprue to ingate). The effect of the liquid metal flow rate and, hence, the mould filling time on air entrainment and inclusion generation has been a controversial topic in the foundry industry for some time. Higher flow rates cause higher velocities in the gating system, but also reduce the time the liquid metal is exposed to oxygen. The pressurisation state or degree the gating system is filled with liquid metal during pouring also depends on the flow rate. The two flow rates that are studied here are $Q_s = 1 \times 10^{-3} \text{ m}^3 \text{ s}^{-1}$ ($t_{\text{fill}} = 20 \text{ s}$) and $Q_s = 0.625 \times 10^{-3} \text{ m}^3 \text{ s}^{-1}$ ($t_{\text{fill}} = 32 \text{ s}$). Air entrainment can also be expected to be affected by the location where the metal stream from the ladle impacts the cone pouring cup. As illustrated in Figure 9(a), a side impact and a centre impact are examined. Finally, the effect of the (head) height of the stream from the ladle above the pouring cup on air entrainment is studied. As can be seen in Figure 9(b), heights of $H = 50.8 \text{ mm}$ (2") and $H = 203.2 \text{ mm}$ (8") are examined. Head heights far in excess of these values are common in the foundry industry, especially when bottom pour ladles are used. Therefore, the present results are only representative of lip pour ladles that are positioned relatively close to the pouring cup. Table 1 shows that all combinations of these cases were simulated, resulting in a total of 16 cases featuring the cone pouring cup with a bottom ingate.

Table 1. Overview of the cases simulated for air entrainment in steel casting.

	Trial	Gating arrangement	Pouring cup/basin	Impact location	Pouring rate, $Q_s \times 10^3$ ($\text{m}^3 \text{ s}^{-1}$)	Head height, H (mm)
Non-pressurised	1	Bottom	Cone cup	Side	1	203.2
	2	Bottom	Cone cup	Side	1	50.8
	3	Bottom	Cone cup	Side	0.625	203.2
	4	Bottom	Cone cup	Side	0.625	50.8
	5	Bottom	Cone cup	Centre	1	203.2
	6	Bottom	Cone cup	Centre	1	50.8
	7	Bottom	Cone cup	Centre	0.625	203.2
	8	Bottom	Cone cup	Centre	0.625	50.8
	9	Bottom	Offset step basin	Side	1	203.2
Pressurised	10	Bottom	Cone cup	Side	1	203.2
	11	Bottom	Cone cup	Side	1	50.8
	12	Bottom	Cone cup	Side	0.625	203.2
	13	Bottom	Cone cup	Side	0.625	50.8
	14	Bottom	Cone cup	Centre	1	203.2
	15	Bottom	Cone cup	Centre	1	50.8
	16	Bottom	Cone cup	Centre	0.625	203.2
	17	Bottom	Cone cup	Centre	0.625	50.8
	18	Bottom	Offset step basin	Side	1	203.2
	19	Side	Cone cup	Side	1	203.2
	20	Top	Cone cup	Side	1	203.2

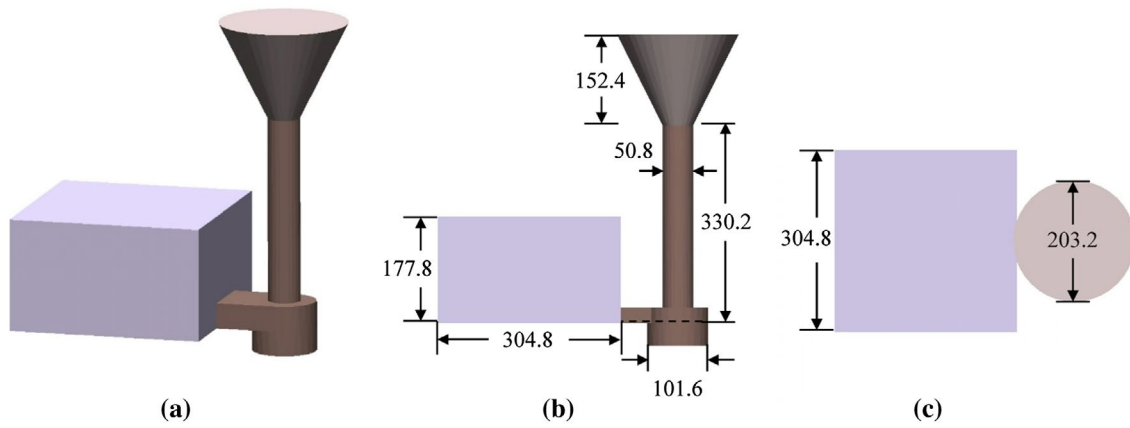


Figure 7. Gating system and casting geometry for the cone pouring cup with bottom ingate cases: (a) isometric view, (b) front view and (c) top view. All dimensions in mm.

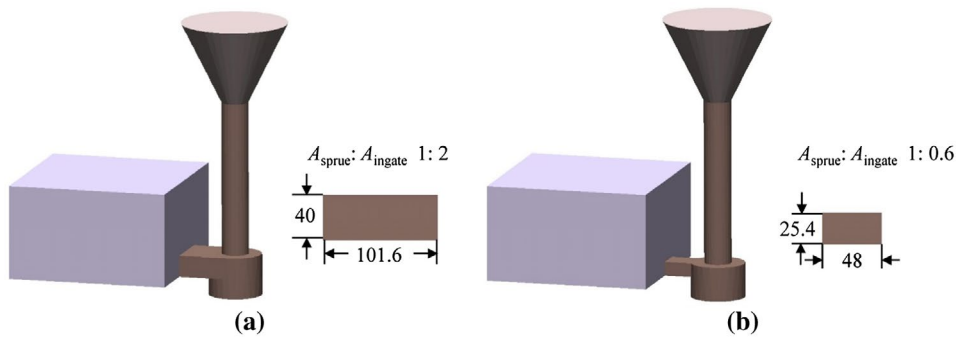


Figure 8. Ingate geometry for (a) the non-pressurised gating system and (b) the pressurised gating system. All dimensions in mm.

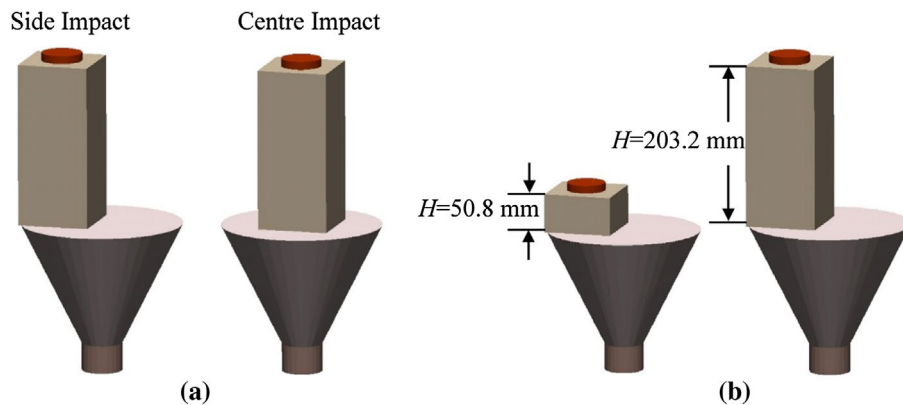


Figure 9. Geometries for (a) the side and centre impact locations and (b) the two different head heights.

Figure 10 shows a comparison of the air entrainment predictions for the non-pressurised and pressurised gating systems. The comparison is made for both side impact (Figure 10(a)) and centre impact (Figure 10(b)). In all cases, the initial impact of the stream from the ladle onto the cone pouring cup (for side impact) or the bottom of the sprue (for centre impact) causes a large spike in the relative air entrainment rate during the first second of filling. This spike is larger for centre impact, because the initial falling height (and, hence, plunging jet velocity) is larger for centre than for side impact. Smaller secondary spikes can be observed at later times,

which can be associated with additional plunging and splashing events. After the initial spike, the air entrainment rate is relatively constant (aside from the fluctuations), although in some cases it decreases slightly until the end of filling. The fluctuations during this period are not due to turbulence of the incoming stream from the ladle, but are generated inside the mould cavity due to unsteadiness of the flow. They are generally larger for the non-pressurised than for the pressurised gating system, indicating that the flow is steadier for a pressurised gating system. Most importantly, during the vast majority of the filling process, the air entrainment rate is significantly

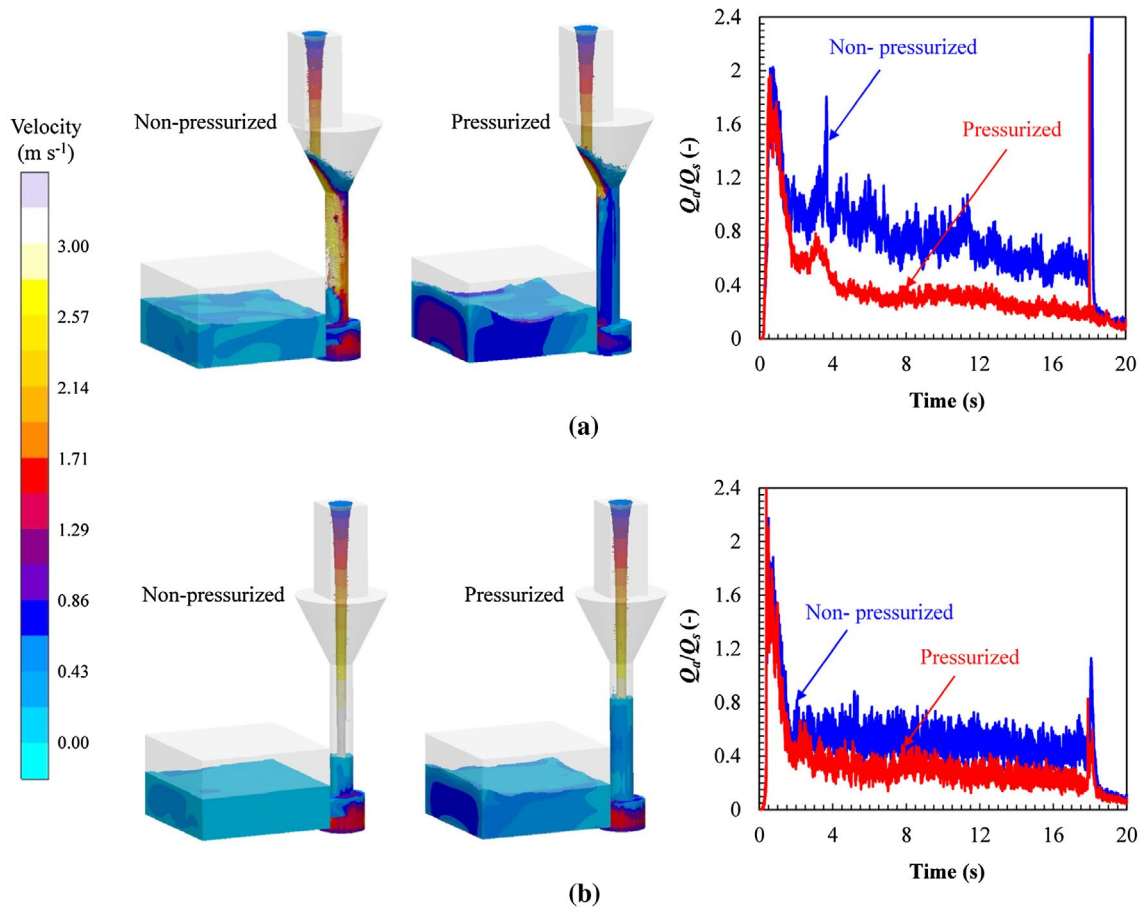


Figure 10. Effect of the gating system pressurisation state on the variation of the relative air entrainment rate (plots on the right) for $Q_s = 1 \times 10^{-3} \text{ m}^3 \text{ s}^{-1}$ ($t_{\text{fill}} = 20 \text{ s}$) and $H = 203.2 \text{ mm}$: (a) side impact, (b) centre impact. The velocity contours are shown at a time of 10 s.

smaller for the pressurised than for the non-pressurised gating system. This can be attributed to the fact that for a pressurised gating system, most of the sprue fills up with liquid metal early during the filling process, causing the falling height from the pouring cup into the sprue to be less on average. A smaller falling height reduces the plunging jet velocity at impact and, hence, the air entrainment rate. For the non-pressurised gating system, the liquid metal level in the sprue is low during the majority of the filling process, resulting in a large falling height, regardless of the impact location.

Figure 11 shows a comparison of the air entrainment predictions for the high and low pouring rates, $Q_s = 1 \times 10^{-3} \text{ m}^3 \text{ s}^{-1}$ ($t_{\text{fill}} = 20 \text{ s}$) and $Q_s = 0.625 \times 10^{-3} \text{ m}^3 \text{ s}^{-1}$ ($t_{\text{fill}} = 32 \text{ s}$), respectively. The comparison is made for the pressurised gating system and both side impact and centre impact. It can be seen that for side impact (Figure 11(a)), the relative air entrainment rate throughout the filling process is lower for the higher pouring rate. This can be attributed to the fact that for the higher flow rate the gating system fills up more quickly with liquid metal. In other words, for the higher flow rate the gating system is more pressurised. For the lower flow rate, the ingate would need to be made smaller to achieve the same pressurisation state as for the higher flow rate. As already explained in connection with Figure 10, a higher pressurisation state causes smaller falling heights and,

hence, smaller velocities and air entrainment rates. For centre impact (Figure 11(b)), the difference in the relative air entrainment rate between the two pouring rates is negligibly small. Hence, the effect of lower velocities due to a lower pouring rate is balanced by the effect of higher velocities in the sprue due to a larger falling height.

Figure 12 shows a comparison of the air entrainment predictions for the small and large head heights of the stream from the ladle above the pouring cup, $H = 50.8$ and $H = 203.2 \text{ mm}$, respectively. The comparison is made for the pressurised gating system, the high flow rate, and both side impact (Figure 12(a)) and centre impact (Figure 12(b)). As expected, a larger head height increases the relative air entrainment rate throughout the pouring process. This can be attributed to a larger falling height causing higher velocities at the point of impact of the stream.

Figure 13 shows a comparison of the total volume of air entrained per volume of steel poured for all 16 cases with a cone pouring cup and a bottom ingate. The following conclusions can be drawn. Side impact of the pouring stream on to the pouring cup significantly increases air entrainment compared to centre impact, where the stream never impacts the pouring cup. Increasing the head height of the ladle above the pouring cup also increases the amount of air entrained. Reducing the filling time has a beneficial effect on air entrainment and

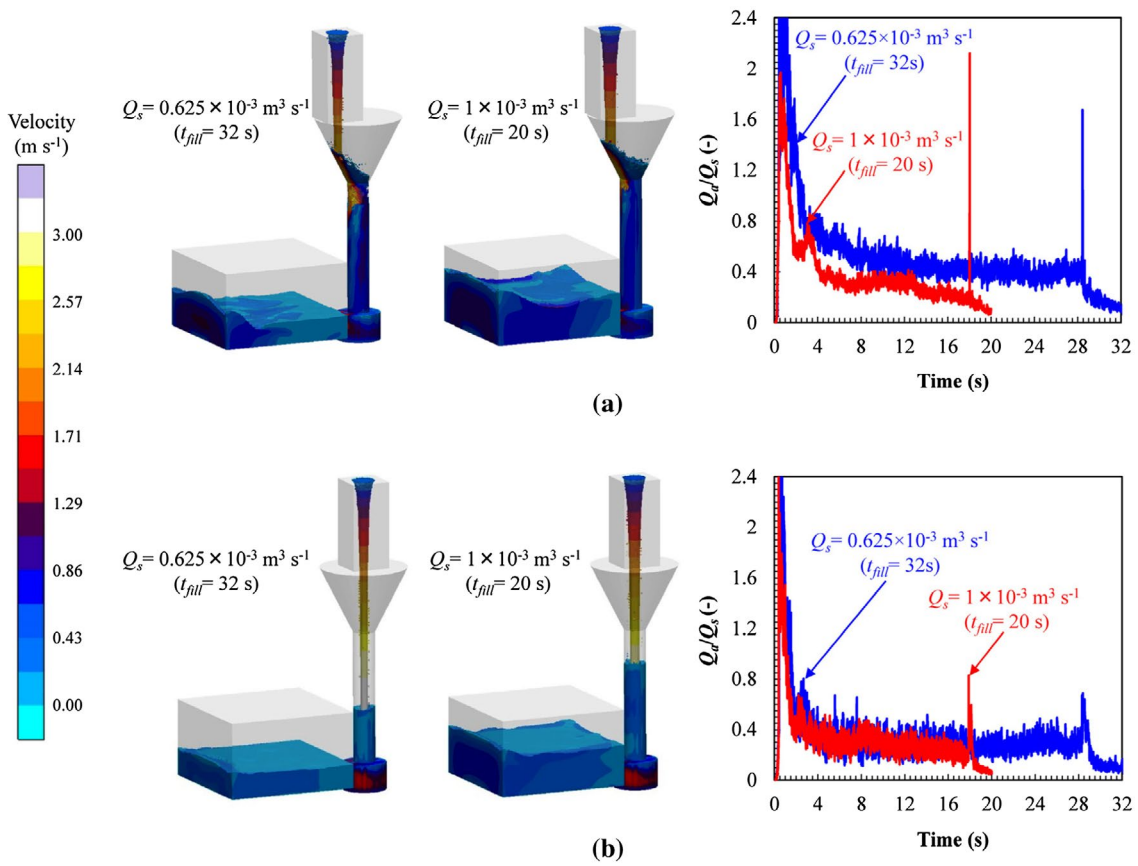


Figure 11. Effect of the liquid metal flow rate, Q_s , on the variation of the relative air entrainment rate (plots on the right) for a pressurised gating system and $H = 203.2$ mm: (a) side impact, (b) centre impact. The velocity contours are shown at a time of 10 s.

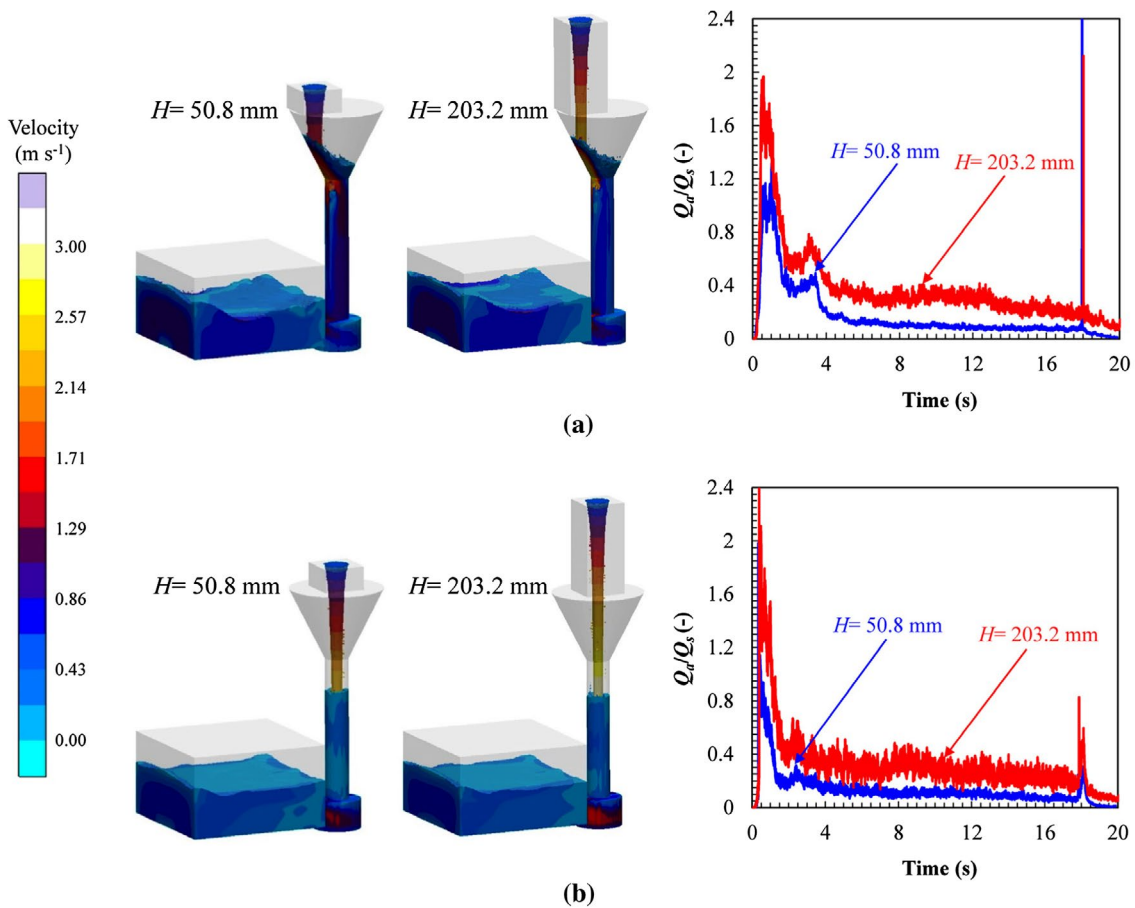


Figure 12. Effect of the head height, H , on the variation of the relative air entrainment rate (plots on the right) for a pressurised gating system and $Q_s = 1 \times 10^{-3} \text{ m}^3 \text{ s}^{-1}$ ($t_{\text{fill}} = 20$ s): (a) side impact, (b) centre impact. The velocity contours are shown at a time of 10 s.

will reduce the amount of inclusions generated. Finally, using a pressurised gating system by minimising the ingate area and keeping the gating system filled with liquid metal throughout the majority of the mould filling process reduces air entrainment. Here, it should be kept in mind that the degree of pressurisation of a given gating system depends on the flow rate during filling (fill time). For centre impact, pressurisation is not nearly as beneficial as for side impact. The merits of gating system pressurisation have also been noted by Campbell [23]. It is important to mention that the amount of air entrained differs by almost a factor of 10 between the best and worst case in Figure 13.

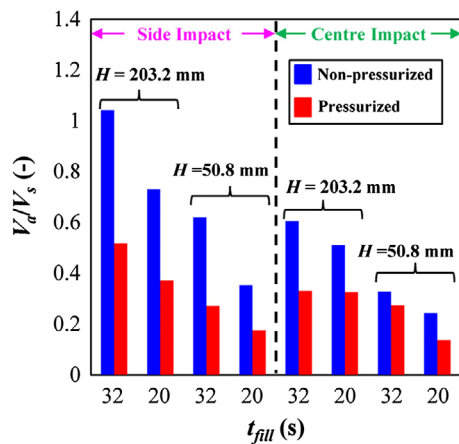


Figure 13. Comparison of the predicted total relative entrained air volumes for the 16 cases with a cone pouring cup and bottom ingate.

Offset step pouring basin

Campbell [23] has suggested the use of an offset step pouring basin in gravity casting to reduce air entrainment. Figure 14 shows a design for an offset step pouring basin that was patterned after Ref. [23] and sized to fit with the present casting. With the present casting simulation code [18], it was not possible to include the highly recommended stopper at the pouring basin exit; hence, the benefits of the use of an offset basin are underestimated. Filling simulations were conducted for the offset step pouring basin with a bottom ingate and $Q_s = 1 \times 10^{-3} \text{ m}^3 \text{ s}^{-1}$ and $H = 203.2 \text{ mm}$.

Figure 15 shows a comparison of the air entrainment rate predictions for the offset step pouring basin with

the cone pouring cup for both side and centre impact. The comparison is made for both the pressurised (Figure 15(b)) and the non-pressurised (Figure 15(c)) gating system. In both cases, the air entrainment rate for the offset step pouring basin is significantly lower than for the cone pouring cup. During the first 4 s of filling, the relative air entrainment rate for the offset step basin shows two peaks. The first peak is due to the metal stream from the ladle impinging onto the offset portion of the basin, while the second peak is due to the liquid metal from the basin plunging into the empty sprue. The fluctuations in the air entrainment rate for the offset step basin are significantly less than for the cone cup, indicating that an offset step basin aids in making the filling flow steadier. Note that the filling process takes about 4 s longer for the offset step basin, since it is larger than the cone cup. Figure 15d shows a comparison of the total volume of entrained air per volume of steel. For the non-pressurised gating system, the use of an offset step basin reduces the amount of entrained air by a factor of about 2 relative to a cone cup with centre impact and a factor of about 3 relative to a cone cup with side impact. For the pressurised gating system, the beneficial effect of the offset step basin is not nearly as strong, but still a factor of about 2 relative to the cone cup with side impact and a factor of about 1.6 relative to the cone cup with centre impact. The conclusion that an offset pouring basin entrains less air compared to a conical pouring cup was also reached in the water modelling study performed by Afsharpour et al. [24].

Ingate location

Gating a casting from the bottom is preferred in the foundry industry, but it requires a relatively long sprue and special moulding techniques (e.g. tiles). Sometimes, the ingates are located on the side of the casting to take advantage of the presence of the mould parting surface. Since the parting surface is usually near the mid-height of the casting, the liquid metal will often fall over considerable heights inside the casting cavity. Such “waterfalls” inside of the mould cavity can be a large source of air entrainment. Clearly, gating a casting from the top is the least desirable configuration from an air entrainment point of view, since it leads to the largest falling heights inside the mould cavity. In order to demonstrate the effect of different ingate locations

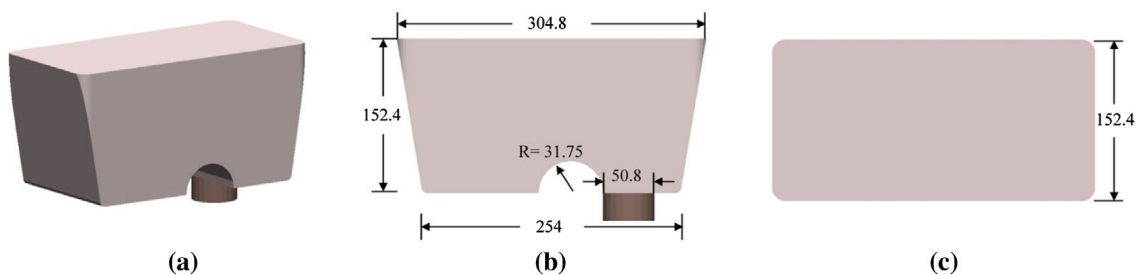


Figure 14. Geometry of the offset step pouring basin: (a) isometric view, (b) front view, and (c) top view. All dimensions in mm.

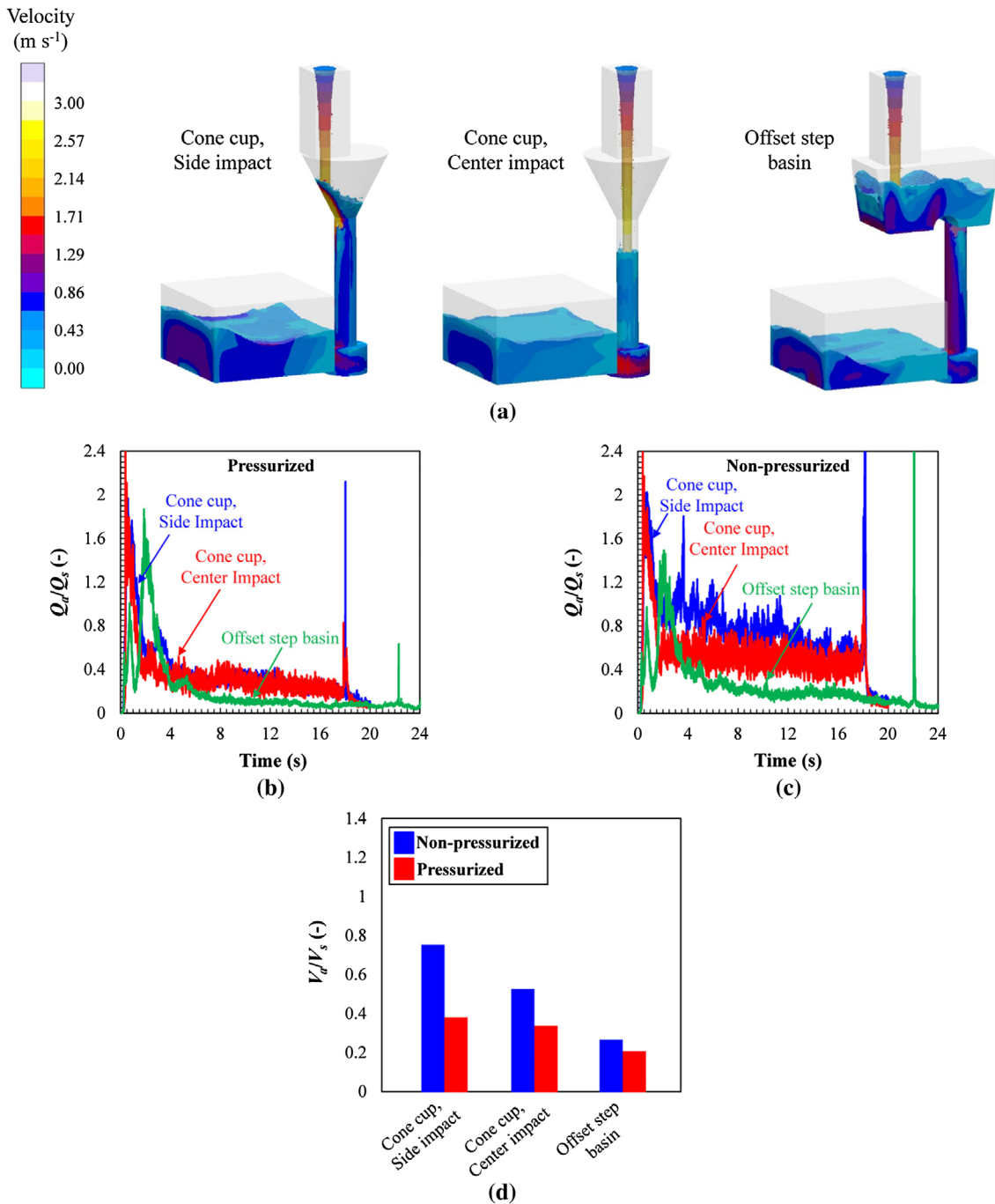


Figure 15. Comparison of the offset step pouring basin with the cone pouring cup (side and centre impact) for $Q_s = 1 \times 10^{-3} \text{ m}^3 \text{ s}^{-1}$ and $H = 203.2 \text{ mm}$: (a) velocity contours at $t = 10 \text{ s}$ for a pressurized gating system, (b) variation of the relative air entrainment rates for a pressurized gating system, (c) variation of the relative air entrainment rates for a non-pressurized gating system and (d) predicted total relative entrained air volumes.

on air entrainment, filling simulations were conducted for the three geometries shown in Figure 16. Figure 16(a) depicts the same bottom-gated casting that was used in the previous parametric studies. The ingate for the casting in Figure 16(b) is located at the mid-height of the casting, while the casting in Figure 16(c) is gated at the top. The length of the sprue and all other features were kept the same for all three ingate locations in order to allow for a more direct comparison between the different cases.

Figure 17 shows a comparison of the air entrainment rate predictions for the three different ingate locations. The comparison is made for the cone pouring cup with side impact, pressurized gating system, $Q_s = 1 \times 10^{-3} \text{ m}^3 \text{ s}^{-1}$ ($t_{\text{fill}} = 20 \text{ s}$), and $H = 203.2 \text{ mm}$. It can be seen that the ingate location significantly affects air entrainment during mould filling. For the side and top-gated castings, a strong jet of liquid metal emanates from the ingate and plunges onto the bottom surface of the casting cavity during large portions of the filling process (Figure

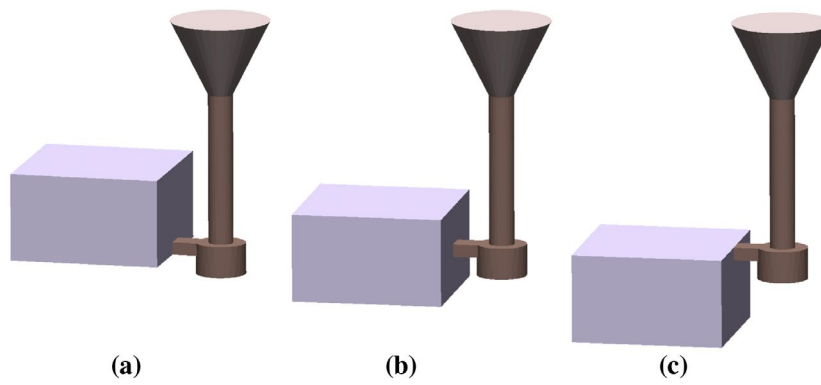


Figure 16. Geometries for the different ingate location cases: (a) bottom gated, (b) side gated and (c) top gated.

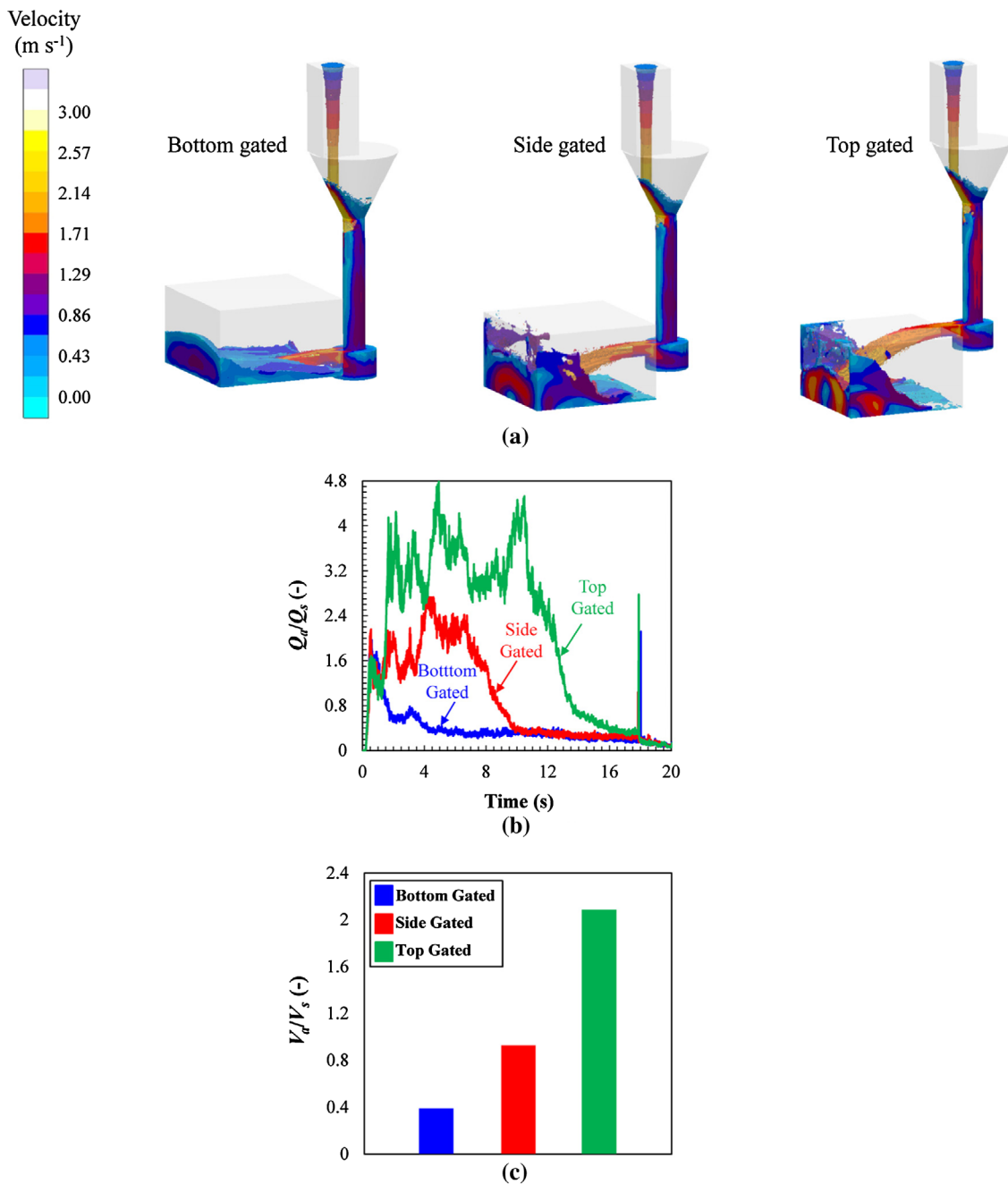


Figure 17. Effect of the ingate location for $Q_s = 1 \times 10^{-3} \text{ m}^3 \text{ s}^{-1}$ ($t_{\text{fill}} = 20 \text{ s}$), $H = 203.2 \text{ mm}$, pressurised gating system, cone pouring cup, and side impact: (a) velocity contours at a time of 4 s, (b) variation of the relative air entrainment rates and (c) comparison of the predicted total relative entrained air volumes.

17(a)). The associated splashing inside of the casting cavity causes very high rates of air entrainment (Figure 17(b)). This air entrainment subsides once the jet from the ingate is fully submerged. Figure 17(c) indicates that the total volume of entrained air for the side ingate is almost 2.5 times larger than for the bottom ingate. For the top ingate, the entrained air volume is more than five times larger than for the bottom ingate. Clearly, to produce clean castings, large “waterfalls” inside of the casting cavity should be avoided.

Conclusion

A model is developed to predict the location and rate of air entrainment as part of a standard mould filling simulation. The local air entrainment rate is calculated as a function of the turbulent kinetic energy and the magnitude of the normal velocity gradient of the liquid metal at the liquid–air interface. The turbulent kinetic energy is estimated using spatial velocity averages, instead of solving a separate turbulence model. The air entrainment model is implemented in a casting simulation software and validated by comparing its predictions to experimental air entrainment measurements for a water jet plunging into a pool. Excellent agreement is obtained over a large range of jet velocities, diameters and turbulence levels.

The model is applied to study the effect of gating system design and pouring parameters on air entrainment in metal casting. It is found that a metal stream from the ladle that is centred above the pouring cup or the use of an offset step pouring basin, low head heights, high flow rates, a pressurised gating system and bottom ingates reduce the amount of entrained air. These results, while realistic, should only be viewed as illustrations of model capabilities. The model may be used in the future to develop general design guidelines for optimised pouring systems that minimise air entrainment. According to Campbell [23], traditional cone-shaped pouring cups, straight down sprues and sprue wells should be avoided altogether. However, due to the geometric complexity and large variation in the size of castings, one cannot expect that general design guidelines are always useful. The computer simulation model developed in this study allows foundries to evaluate different gating designs and pouring parameters for each individual casting.

Future work will also include further experimental validation of the air entrainment model. The present model was calibrated for a plunging water jet only. It is not entirely clear if it provides quantitatively accurate air entrainment predictions for other flow configurations (e.g. breaking waves) and for liquid metals. Furthermore, the present model will be linked to an inclusion generation and transport model, in a manner similar to the one by Melendez et al. [25]. Using such a combined model allows for the prediction of the final oxide inclusion sizes, number densities and locations in a solidified casting.

Disclosure statement

No potential conflict of interest was reported by the authors.

ORCID

Seyyed Hojjat Majidi  <http://orcid.org/0000-0003-2351-2095>

References

- [1] Belden J, Ravela S, Truscott T, et al. Bubble fields in 3D (no glasses necessary). Abstract presented at: 64th Annual Meeting of the APS Division of Fluid Dynamics; 2011 November 20–22; Baltimore (MD).
- [2] Moraga FJ, Carrica PM, Drew DA, et al. A sub-grid air entrainment model for breaking bow waves and naval surface ships. *Comput Fluids*. 2008;37:281–298.
- [3] Ma J, Oberai AA, Drew DA, et al. A quantitative sub-grid air entrainment model for bubbly flows – plunging jets. *Comput Fluids*. 2010;39:77–86.
- [4] Shi F, Kirby JT, Ma G. Modeling quiescent phase transport of air bubbles induced by breaking waves. *Ocean Model*. 2010;35:105–117.
- [5] Xiang M, Cheung SCP, Tu JY, et al. A multi-fluid modelling approach for the air entrainment and internal bubbly flow region in hydraulic jumps. *Ocean Eng*. 2014;91:51–63.
- [6] Ma J, Oberai AA, Drew DA, et al. A comprehensive sub-grid air entrainment model for RANS modeling of free-surface bubbly flows. *J Comp Multiphase Flow*. 2011;3:41–56.
- [7] Ma J, Oberai AA, Lahey RT, et al. Modeling air entrainment and transport in a hydraulic jump using two-fluid RANS and DES turbulence models. *Heat Mass Transfer*. 2011;47:911–919.
- [8] Ma J, Oberai AA, Drew DA, et al. A two-way coupled polydispersed two-fluid model for the simulation of air entrainment beneath a plunging liquid jet. *J Fluids Eng*. 2012;134:101304.
- [9] Souders DT, Hirt CW. Proceedings of the world water and environmental resources congress: critical transitions in water and environmental resources management; 2004 June 27–July 1; Salt Lake City (UT); USA.
- [10] Flow3D, Santa Fe, (NM): Flow Science
- [11] Campbell J. Entrainment defects. *Mater Sci Technol*. 2006;22:127–145.
- [12] Lai NW, Griffiths WD, Campbell J. Proceedings of the 13th International Conference on Modeling of Casting, Welding and Advanced Solidification Processes X; 2003 May 25–30; Warrendale (PA): TMS.
- [13] Reilly C, Green NR, Jolly MR. The present state of modeling entrainment defects in the shape casting process. *Appl Math Model*. 2013;37:611–628.
- [14] Cuesta R, Delgado A, Maroto A, et al. Numerical modelling oxide entrainment in the filling of castings: the effect of the Weber number. *JOM*. 2006;58:62–65.
- [15] Yang X, Huang X, Dai X, et al. Numerical modelling of entrainment of oxide film defects in filling of aluminium alloy castings. *Int J Cast Met Res*. 2004;17:321–331.
- [16] Reilly C, Green NR, Jolly MR, et al. The modelling of oxide film entrainment in casting systems using computational modelling. *Appl Math Model*. 2013;37:8451–8466.
- [17] Yue Y. Modelling of the effects of entrainment defects on mechanical properties in Al–Si–Mg alloy castings [dissertation]. Birmingham (UK): University of Birmingham; 2014.
- [18] MAGMAsoft, MAGMA GmbH, Aachen.
- [19] Hunt J. Turbulent structure and turbulent diffusion near gas–liquid interfaces. In: Brutsaert W, Jirka G, editors.

- Gas transfer at water surfaces. Dordrecht: Reidel; 1984. p. 67–82.
- [20] Sene KJ. Air entrainment by plunging jets. *Chem Eng Sci.* 1988;43:2615–2623.
- [21] Kobus H. Symposium on scale effects in modelling hydraulic structures; 1984 September 3–6; Stuttgart: Inst. Für Wasserbau. p. 1–10.
- [22] Ervine DA, McKeough E, Elsayy EW. Effect of turbulence intensity on the rate of air entrainment by plunging water jets. *Proc Inst Civil Eng.* 1980;69:425–445.
- [23] Campbell J. Complete casting handbook: metal casting processes, techniques and design. Oxford (UK): Butterworth-Heinemann; 2011.
- [24] Afsharpour M, Homayun B, Boutorabi SMA. Water modelling of effects of pouring basin and sprue geometry on entrance of air bubbles into mould. *Mater Sci Technol.* 2014;30:152–159.
- [25] Melendez AJ, Carlson KD, Beckermann C. Modelling of reoxidation inclusion formation in steel casting. *Int J Cast Met Res.* 2010;23:278–288.